Extrapolated full waveform inversion: An image-space approach

Yunyue Elita Li, National University of Singapore, and Laurent Demanet, Massachusetts Institute of Technology

SUMMARY

The primary factor that prevents full waveform inversion from universal success is the band-limited nature of seismic data, resulting in a gap between the low wavenumber background velocity model and the high wavenumber seismic images. In this paper, we propose to bridge the wavenumber gap in the extended image space, where full kinematic information in the data is preserved in spite of the inaccuracy of the background migration velocity model, and where the wavenumber range of the extended image is extrapolated using total-variation constrained deconvolution. This explicit wavenumber extrapolation is nested within least-squares reverse time migration iterations to ensure that the resulting extended images match the recorded band-limited data. We then synthesize reflection data using extended Born modeling with the extrapolated images. Numerical experiments show that although the total variation projection has limited the high frequencies that can be recreated by extended Born modeling, the low frequencies are reliably extrapolated at all offsets, given a reasonable starting velocity model. When the initial model is too crude, the proposed frequency extrapolation breaks down near the complex structures.

INTRODUCTION

The extended imaging scheme introduces extra spatial or time lags in the image space to accommodate the kinematic error that has not been modeled correctly by the migration velocity model (Rickett and Sava, 2002; Sava and Fomel, 2006). When the initial velocity is inaccurate, the images in the extended model space will not focus at the zero subsurface-offset or at zero time-lag, as opposed to the assumption by conventional RTM. These "leaked" events in the extended model space help reconstruct the accurate kinematics of the recorded reflection data via extended Born modeling, regardless of the accuracy of the migration velocity model. A conceptual description of the extended Born modeling operator takes the form

$$\hat{d} = F_e(w)I_e, \tag{1}$$

where F_e is the extended Born modeling operator, the adjoint operator of the extended imaging operator; I_e is the extended image, and $\hat{d}$ is the modeled data. Since the kinematics in $\hat{d}$ match the kinematics in the recorded reflection data d, the extended images can be used to fit the recorded reflection data without the concerns of cycle-skipping in conventional full waveform inversion (Gauthier et al., 1986; Gerhard Pratt et al., 1998; Pratt and Shipp, 1999a,b; Etgen et al., 2009). The resulting iterative inversion scheme is referred as least-squares extended reverse time migration (LSERTM). LSERTM has shown robustness against the inaccuracies in the migration velocity model in many applications, such as to separate contaminated seismic records with simultaneous sources (Leader et al., 2014), to enhance the signal-to-noise ratio, and to interpolate the prestack seismic data (Weibull and Arntsen, 2014; Hou and Symes, 2016).

Here, we focus on the wavenumber (and corresponding frequency) analysis of the extended images (and corresponding data). After extended Born modeling, the frequency band of the synthesized data $\hat{d}$ is determined by two factors: the frequency band of the source wavelet w defined in the modeling operator F_e, and the wavenumber band of the extended image I_e. The key innovation of this paper can be summarized mathematically as follows:

$$\hat{d}_l = F_e(w_l)\Delta m_e, \tag{2}$$

where Δm_e is the extended model, a modified version of I_e with same kinematical information but a wider wavenumber range; w_l is a synthesized wavelet, whose frequency support is wider than the original source wavelet w; and $\hat{d}_l$ is the newly synthesized data, whose frequency support is also wider than the original recorded data d. In other words, frequency extrapolation of the data is achieved by wavenumber extrapolation of the extended images and subsequent extended Born modeling.

The wavenumber extrapolation is an essential step in the frequency extrapolation, because the raw extended images only contain wavenumber components that are supported by the frequency band of the recorded data. In this paper, we propose to perform wavenumber extrapolation by adding a total variation (TV) constraint (Rudin et al., 1992; Fadili and Peyré, 2011) to the LSERTM inversion. However, the extended Born modeling and imaging operators are too expensive to evaluate for hundreds of iterations that are required for the TV constraint. Therefore, we design a variable-wavelet 1D convolutional operator to approximate the expensive normal operator $F_e^* F_e$ and solve the TV-constrained deconvolution problem as a preconditioning step of the LSERTM iterations. This deconvolution step also compensates the footprint of the wavelet on the extended images. Consequently, we achieve fast convergence for both wavenumber extrapolation and data fitting by extended Born modeling.

The spirit of this paper is aligned with our previous papers (Li and Demanet, 2015, 2016): low frequency data can be synthesized based on the bandlimited recorded data. The full waveform inversion schemes based on the extrapolated low frequencies are referred as extrapolated full waveform inversion (EFWI) in both cases. However, the particular approaches are drastically different. The previously proposed phase tracking method is performed in the data space, via highly controlled model parameterization and strong model reduction. The method we propose in this paper achieves a similar goal in the image space, via image extension and deconvolutive frequency extrapolation. The implicit duality between these two methods is yet to be explored.

METHOD

To illustrate the workflow of the proposed method, we demonstrate each step using a simple three-layer synthetic example (Figure 1(a)). The background velocity is 2000 m/s and the velocity of the middle layer is 4000 m/s. The thickness of the middle layer is 200 m. Figure 1(b) shows the bandlimited shot record between 6 and 50 Hz at $x_s = 0$ m. We use 41 shots at 100 m spacing to image the synthetic model.

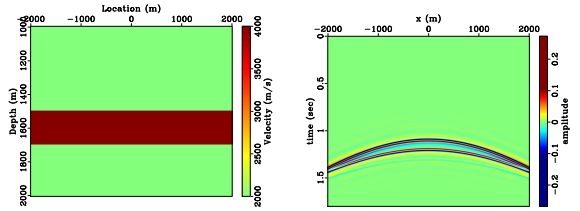

(a) (b)

Figure 1: (a) The synthetic model with a high-velocity layer. (b) Synthetic seismic data recorded between (6-50 Hz).

Least-squares extended reverse time migration (LSERTM)

The primary reflection data can be estimated by Born approximation using the causal Green's function $G(\mathbf{x},\mathbf{y},t)$ for a given background velocity m_0. Hence, the resulting scattered data modeled by the Born modeling operator can be expressed:

$$\begin{aligned}(F\Delta m)(\mathbf{x_s},\mathbf{x_r},t) &= \frac{\partial^2}{\partial t^2}\int d\mathbf{x}d\tau w(\tau)G(\mathbf{x_s},\mathbf{x},\tau)\\ &\times\ 2m_0(\mathbf{x})\Delta m(\mathbf{x})G(\mathbf{x},\mathbf{x_r},t-\tau), \quad (3)\end{aligned}$$

with $w(t)$ a source wavelet that is bandlimited to the frequency content of the data and Δm the perturbation to the background velocity. The adjoint operator F^* maps scattered data δd to the model space:

$$\begin{aligned}(F^*\delta d)(\mathbf{x}) &= 2m_0(\mathbf{x})\int d\mathbf{x_s}d\mathbf{x_r}dtd\tau w(\tau)G(\mathbf{x_s},\mathbf{x},\tau)\\ &\times\ G(\mathbf{x},\mathbf{x_r},t-\tau)\frac{\partial^2}{\partial t^2}\delta d(\mathbf{x_s},\mathbf{x_r},t). \quad (4)\end{aligned}$$

The model space object in Equation 4 is often referred as a reverse-time migration image.

Based on the survey-sinking imaging condition introduced by Claerbout (1985), we can introduce an extra subsurface offset to the migration image. The resulting imaging operator is referred as the extended imaging operator F_e^* which maps the scattered data to the extended images:

$$\begin{aligned}I(\mathbf{x},\mathbf{h}) &= (F_e^*\delta d)(\mathbf{x},\mathbf{h})\\ &= 2m_0(\mathbf{x})\int d\mathbf{x_s}d\mathbf{x_r}dtd\tau w(\tau)G(\mathbf{x_s},\mathbf{x}+\mathbf{h},\tau)\\ &\times\ G(\mathbf{x}-\mathbf{h},\mathbf{x_r},t-\tau)\frac{\partial^2}{\partial t^2}\delta d(\mathbf{x_s},\mathbf{x_r},t). \quad (5)\end{aligned}$$

The adjoint operator F_e is referred as the extended Born modeling operator which maps the extended images to the scattered data:

$$\begin{aligned}\delta\hat{d}(\mathbf{x_s},\mathbf{x_r},t) &= (F_e\Delta m_e)(\mathbf{x_s},\mathbf{x_r},t)\\ &= \frac{\partial^2}{\partial t^2}\int d\mathbf{x}d\mathbf{h}d\tau w(\tau)G(\mathbf{x_s},\mathbf{x}+\mathbf{h},\tau)\\ &\times\ 2m_0(\mathbf{x})\Delta m_e(\mathbf{x},\mathbf{h})G(\mathbf{x}-\mathbf{h},\mathbf{x_r},t-\tau). \quad (6)\end{aligned}$$

Under favorable conditions, this pair of forward and adjoint operators are pseudodifferential. In that case, sequentially applying them one after the other, regardless of the order, does not move the singularities. Therefore, the phases modeled by sequential application of this pair of operators are aligned with the original object. The amplitude differences can be compensated by gradient-based inversion due to linearity. ten Kroode (2012) and Hou and Symes (2015) provided detailed explanations for the statement above and proposed designs of pseudoinverse operators for the extended Born modeling in terms of Kirchhoff migration and reverse-time migration, respectively.

In this paper, we formulate least-squares extended reverse time migration problem explicitly:

$$J_{LSERTM}(\Delta m_e(\mathbf{x},\mathbf{h})) = \frac{1}{2}\sum_{r,s,t}(\delta u_s(\mathbf{x_s},\mathbf{x_r},t;\Delta m_e) - \delta d_{r,s,t})^2, \quad (7)$$

where δd is the primary reflection data, and δu_s is the modeled data by Equation 6. When working with reflection data whose specular angle is limited to a maximum of 45°, the LSERTM inversion can only resolve the wavenumber components corresponding to the frequency content of the data.

Figure 2(a) shows the extended image obtained by migrating the reflection seismic data using a constant velocity model of 2200 m/s. Due to the too fast migration velocity, the reflectors are imaged deeper than their true depth. The upward curvature and strong energy at $h \neq 0$ in the subsurface offset domain indicates that the migration velocity is inaccurate. Similarly, Figure 2(b) shows the extended image when a constant migration velocity of 1800 m/s is used. The reflectors are imaged shallower with strong curvatures in the subsurface offset domain. In both cases, the leaked energy in the subsurface offset domain preserves the kinematic information of the seismic data. The wavenumber contents in both extended images are consistent with the frequency contents in the recorded data, leading to low resolution images of the true model.

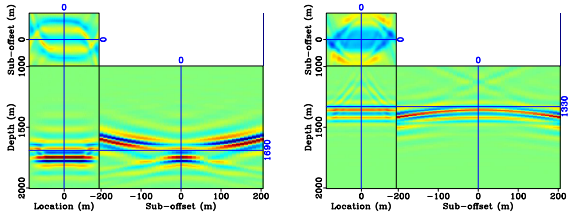

(a) (b)

Figure 2: Extended images obtained by LSERTM, using a constant fast velocity mode in (a) and using a constant slow velocity model in (b).

Preconditioning with total variation constrained deconvolution

This inverse problem in Equation 7 has a large nullspace due to the incompleteness of data in space and frequency. To better constrain the inverse problem and to honor the geological information, we introduce a total variation (TV) regularization to augment the inversion:

$$\begin{aligned} \min \quad & ||F_e \Delta m_e(\mathbf{x},\mathbf{h}) - \delta d_{r,s,t}||_2^2, \\ \text{s.t.} \quad & ||\Delta m_e||_{\text{TV}} \leq \tau, \end{aligned} \tag{8}$$

where $||\cdot||_{\text{TV}}$ denotes the TV norm (morally, the L^1 norm of the gradient), and τ is a user-defined parameter. The top equation in the fitting system is the same as Equation 7. Solving a TV constrained problem requires too many iterations for the computational cost of LSERTM to be affordable. Hence, we rearrange the optimization goals:

$$\begin{aligned} \min \quad & ||F_e^* F_e \Delta m_e(\mathbf{x},\mathbf{h}) - F_e^* \delta d||_2^2, \\ \text{s.t.} \quad & ||\Delta m_e||_{\text{TV}} \leq \tau. \end{aligned} \tag{9}$$

The object $F_e^* \delta d$ is already defined in Equation 5 as the extended image $I(\mathbf{x},\mathbf{h})$. We now approximate the normal operator using a cheap 1-D convolution operator $A \approx F_e^* F_e$ and obtain an approximated system of equations to solve for the TV constrained optimization problem:

$$\begin{aligned} \min \quad & ||A\Delta m_e(\mathbf{x},\mathbf{h}) - I(\mathbf{x},\mathbf{h})||_2^2, \\ \text{s.t.} \quad & ||\Delta m_e||_{\text{TV}} \leq \tau. \end{aligned} \tag{10}$$

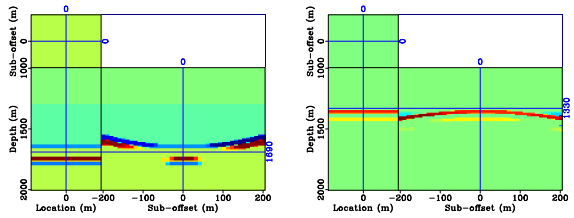

Figure 3: Extended images obtained by LSERTM preconditioned by TV-constrained deconvolution, using a constant fast velocity model in (a) and using a constant slow velocity model in (b).

Notice that the deconvolution problem in Equation 10 is performed in the depth domain, where the seismic wavelet is stretched due to velocity variation and variable illumination. Conventional stationary wavelet deconvolution as performed in the time domain is insufficient to capture the source signature for all depth ranges. Therefore, we design a velocity-dependent variable wavelet deconvolution operator A to better approximate the extended normal operator $F_e^* F_e$.

To solve the TV constrained inverse problem, we use a projected gradient descent method, which projects the updated model after each iteration to a total variation ball of finite radius:

$$\Delta m_e^{i+1} = \text{Proj}_{\{||\cdot||_{\text{TV}} \leq \tau\}} \left(\Delta m_e^i + \alpha A^* (I - A\Delta m_e^i) \right), \tag{11}$$

where $\text{Proj}_{\{||\cdot||_{\text{TV}} \leq \tau\}}$ is the projector on the TV ball and α is a predetermined step length.

Figure 3 shows the extended images obtained by LSERTM with TV-constrained deconvolution preconditioning. Compared with the extended images in Figure 2, preconditioned LSERTM not only removes the migration artifacts from the image, but also extends the bandwidth in wavenumber way beyond the wavenumber supported by the frequencies in the data. The preconditioning will also speed up the convergence of LSERTM.

Figure 4 compares the wavenumber spectra of the true model (in blue), the extended images (in green), and the extended images after TV-constrained deconvolution (in red). The original image does not contain any low wavenumber components due to the missing low frequencies in the data. Although the image after TV-LSERTM does not reproduce the spectrum of the true model exactly, it has restored the relative balance between the low wavenumber and the high wavenumber components.

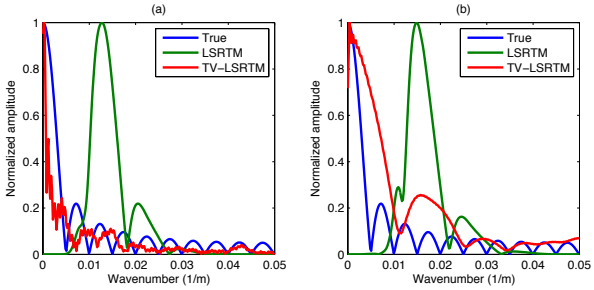

Figure 4: Comparison of average wavenumber spectra of the true model (Blue), of the inverted image (Green) by LSERTM, and of the image by LSERTM preconditioned by TV-constrained deconvolution (Red), for the cases of constant fast velocity (a) and constant slow velocity (b).

Figure 5 compares the low frequency (0 - 6 Hz) seismic records reconstructed by extended Born modeling with the data record modeled using the true velocity model. Both phase and amplitude of the low frequency data have been successfully reconstructed, despite the inaccuracies in the migration velocity model. Slight phase differences at large offsets are due to the differences in the boundary reflections.

At this point, the low frequency data are reconstructed using the extended linearization scheme preconditioned by wavenumber-extending deconvolution. After filling in the frequency gap, the conventional Born linearization at the low frequencies is accurate enough to be used for updating the background (low-wavenumber) velocity model m_0. Therefore, the synthesized data can provide coherent information for full waveform inversion when sweeping over data from low to high frequencies. The resulting model from FWI contains a full wavenumber spectrum, eliminating the need of interpreting velocity and reflectivity models separately.

Extrapolated full waveform inversion

To demonstrate the reliability of the extrapolated low frequency data, we use the reconstructed low frequencies to initialize the

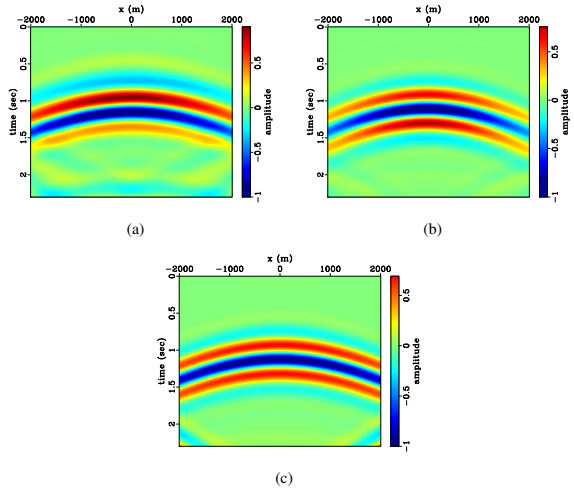

Figure 5: Comparison of low frequency (0-6 Hz) seismic record. (a) Data record reconstructed from the constant fast velocity and extended image in Figure 3(a). (b) Data record reconstructed from the constant slow velocity and extended image in Figure 3(b). (c) Data record modeled using the true velocity model in Figure 1(a).

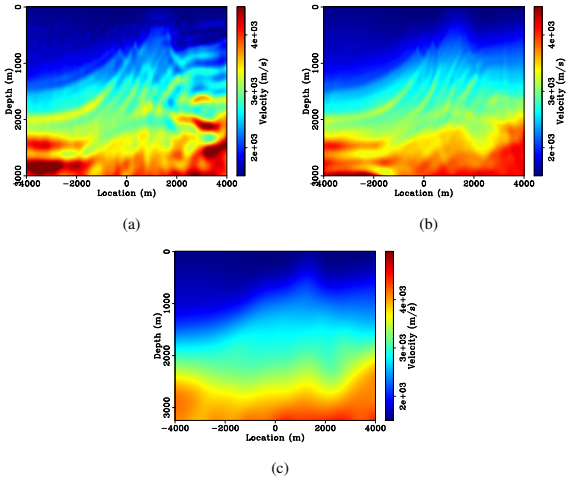

Figure 6: (a) Low wavenumber model by inverting modeled data at low frequencies (2-6 Hz). (b) Low wavenumber model by reconstructed data via extended Born modeling at low frequencies (2-6 Hz). (c) Initial model (maximum wavenumber corresponds to 2 Hz).

frequency sweep of full waveform inversion on the Marmousi model. The initial model we use for the numerical test represents a typical case when the low-wavenumber velocity model is obtained by ray-based tomography or wave-equation migration velocity analysis: the kinematics of seismic data are accurately explained up to 2 Hz, which is still lower than the lowest frequency recorded (6 Hz) in the data. The highest available frequency in the data for extrapolation is 50 Hz.

Figure 6 compares the low wavenumber models inverted from modeled low frequency (2 - 6 Hz) data (a) and from the extrapolated low frequency (2 - 6 Hz) data (b) with the smooth initial model in (c). The inverted model from extrapolated data appears to be higher resolution than the inverted model from modeled data; however, this apparent higher resolution is due to the unbalanced frequency components in the data. Nonetheless, the extrapolated data provide reliable information in the frequency gap between 2 Hz and 6 Hz, which maps to reasonable estimations of the model. Both of these models can be used to initialize FWI at higher frequencies (6 Hz and above).

DISCUSSIONS AND CONCLUSIONS

We have proposed two different methods to synthesize the low frequency data from the bandlimited field recordings. In the previously phase tracking method (Li and Demanet, 2015, 2016), the low frequency data are estimated in the data space as a pure data processing step, hence the accuracy of which is independent of the accuracy of the initial velocity model. Accuracy of the extrapolated low frequencies by phase tracking is in general higher for near offsets than for far offsets, due to higher signal amplitudes at near offsets. Phase tracking becomes ambiguous at large offsets where weak crossing events are contaminated by noise. Consequently, we have limited the application of the current version of the phase tracking algorithm to near offsets (< 500 m).

On the other hand, the accuracy of the image-space method we proposed here is relatively uniform for all offsets and more robust to the noise in the data, not only because of the multifold stacking at each image point, but also because of the denoising effect of the TV constraints. The main drawback of the image-space method is that its accuracy relies on the accuracy of the initial velocity model. Numerical experience shows that the low frequencies extrapolated after TV-constrained deconvolution become unreliable when the initial velocity is too crude, especially in regions where the geological environment is highly complex. Comparing with the phase-tracking method which extracts explicit handles of extrapolated phase and amplitude, the wavenumber extrapolation by TV deconvolution is more automatic and implicit. Therefore, further studies are needed to improve the stability of the wavenumber extrapolation when the background velocity is less accurate.

In general, the image-space method is more computational intensive than the data-space method. Nonetheless, the reconstructed data by the image-space method is more consistent between the extrapolated low frequency and the recorded high frequency. Consequently, the reconstructed data can be used throughout the frequency sweep of FWI after extrapolation.

ACKNOWLEDGEMENTS

This project was funded in part by Total SA. LD is also funded by AFOSR grants FA9550-12-1-0328 and FA9550-15-1-0078, ONR grant N00014-16-1-2122, NSF grant DMS-1255203. Yunyue Elita Li acknowledges the MOE Tier-1 Grant R-302-000-165-133 for financial support.

REFERENCES

Claerbout, J. F., 1985, Fundamentals of geophysical data processing: Pennwell Books, Tulsa, OK.

Etgen, J., S. H. Gray, and Y. Zhang, 2009, An overview of depth imaging in exploration geophysics: Geophysics, **74**, WCC1.

Fadili, J. M., and G. Peyré, 2011, Total variation projection with first order schemes: IEEE Transactions on Image Processing, **20**, 657–669.

Gauthier, O., J. Virieux, and A. Tarantola, 1986, Two-dimensional nonlinear inversion of seismic waveforms: Numerical results: Geophysics, **51**, 1387.

Gerhard Pratt, C. Shin, and Hicks, 1998, Gauss-Newton and full Newton methods in frequency-space seismic waveform inversion: Geophysical Journal International, **133**, 341–362.

Hou, J., and W. W. Symes, 2015, An approximate inverse to the extended Born modeling operator: Geophysics, **80**, R331–R349.

———, 2016, Accelerating extended least-squares migration with weighted conjugate gradient iteration: Geophysics, **81**, S165–S179.

Leader, C., B. Biondi, et al., 2014, Demigration and image space separation of simultaneously acquired data: 2014 SEG Annual Meeting.

Li, Y. E., and L. Demanet, 2015, Phase and amplitude tracking for seismic event separation: Geophysics, **200**, 363–373.

———, 2016, Full waveform inversion with extrapolated low frequency data: Geophysics, **81**, R339–R348.

Pratt, R. G., and R. M. Shipp, 1999a, Seismic waveform inversion in the frequency domain; Part 2; Fault delineation in sediments using crosshole data: Geophysics, **64**, 902–914.

———, 1999b, Seismic waveform inversion in the frequency domain; Part 2; Fault delineation in sediments using crosshole data.

Rickett, J. E., and P. C. Sava, 2002, Offset and angle-domain common image-point gathers for shot-profile migration: Geophysics, **67**, 883–889.

Rudin, L. I., S. Osher, and E. Fatemi, 1992, Nonlinear total variation based noise removal algorithms: international symposium on physical design, **60**, 259–268.

Sava, P., and S. Fomel, 2006, Time-shift imaging condition in seismic migration: Geophysics, **71**, S209–S217.

ten Kroode, F., 2012, A wave-equation-based Kirchhoff operator: Inverse Problems, **28**, 115013 – 115040.

Weibull, W. W., and B. Arntsen, 2014, Reverse-time demigration using the extended-imaging condition: Geophysics, **79**, WA97–WA105.